Modeling and Experimental Validation of a Planar Microconveyor Based on a 2 x 2 Array of Digital Electromagnetic Actuators

Simon Duque Tisnes, Laurent Petit, Christine Prelle, Frederic Lamarque

Modeling and Experimental Validation of a Planar Microconveyor Based on a 2 × 2 Array of Digital Electromagnetic Actuators

Simón Duque Tisnés , Laurent Petit , Christine Prelle , and Frédéric Lamarque

***Abstract*—A critical component of the highly packaged and automated environment of the microfactory is its transportation system. It needs to be autonomous, flexible, precise and, crucially, easy to integrate given the compact and dense nature of the microfactory. In this article, we present the modeling and experimental validation of a digital actuator array used as a stick-slip microconveyance system. This array is based on a modular and scalable design of a 2×2 matrix of electromagnetic digital actuators working in open-loop collaboration to perform planar conveyance tasks while being easy to integrate. A dynamic model of the array was developed and compared with experimental measurements of the mobile parts kinematics, unidimensional and bidimensional conveyed object displacements. The experimental measurements were taken with a dual camera setup—one for the position measurements of the conveyed object and a high-speed camera at 15 kHz for the kinematics of the mobile parts of the actuators and conveyed object. From the experimental tests, we measured a minimum and maximum object displacement step of 7.9 and 204.5 μm, respectively. The minimum rise time of the digital actuator was 0.8 ms. The bidimensional movements of the object demonstrated the planar motion capacity of the array, with generated angles from 1°to 88°. The dynamic model achieved a good correlation with the experimental measurements of the mobile part of the actuator as well as the conveyed object. The open-loop control performance of our digital actuation system suggests an interesting alternative to the conveyance systems for the microfactory.**

***Index Terms*—Collaborative actuation, conveyance system, digital actuator, electromagnetic actuator, MEMS array, microfactory, planar motion, smart surface.**

This work was supported by a public grant overseen by the French National Research Agency (ANR) as part of the Tridimensional Microconveyance Systems for Microfactory Program under Grant ANR-15-CE10-0002-01.

The authors are with the CNRS, Roberval (Mechanics energy and electricity), Universite de Technologie de Compiègne, 60203 Compiègne, France (e-mail: saimonduque@gmail.com; laurent.petit@utc.fr; christine.prelle@utc.fr; frederic.lamarque@utc.fr).

I. Introduction

MINIATURIZATION has, and will, yield important theoretical, technological, and application progresses such as micromechanics theory, microfabrication techniques and microsurgery, microsatellites, and Internet of Things (IoT). For the construction of the components of such systems a logical approach is to implement a factory proportional to the size of the produced items; thus the concept of microfactory was born [1]. In this highly packaged and automated microfactory, the miniature size of the machining and sensing tools reduces the production cost, notably the energy consumption. A critical part of any microfactory is its transportation system: from raw material to final product, multiple parts need to be conveyed between different machining stations and quality control stages until the desired product is finished. These conveyance systems need to be autonomous, flexible, precise, and easy to integrate given the compact and dense nature of the microfactory.

The conveyance systems based on a continuous or analogical actuator use closed-loop controls to reach high performance levels, thus needing high precision sensors and making their integration complex. As an alternative, conveyance systems based on a collaboration of digital actuators are integrated in a simpler way [2]. These digital actuators transport objects with a series of transitional states. Digital actuators are composed of a mobile part able to switch between well-known and repeatable discrete positions. Energy is only required to switch between these discrete positions and no energy is needed to maintain them at their discrete positions. The repeatability in initial and final position of the digital actuators allows the conveyor to be implemented in open loop. This avoids the need for sensors and simplifies the system's integration. The open-loop control enables the use of simple pulsing signals, reducing the complexity of the control. Also, digital microconveyance systems could be implemented in modules, easing the task of extending the microfactory by adding modules and increasing its flexibility and reconfigurability [3]. On the other hand, the fabrication process of the actuator is a critical issue as it defines the actuator stroke. Also, the displacement of the conveyed object is obtained step by step and the displacement smoothness relies on the actuator physical principle and step resolution.

Multiple micrometer conveyance systems have been reported in the literature. They can be described in terms of the energy type of their actuation system such as pneumatic [4]–[10],

electrostatic [11], [12], piezoelectric [13], [14], electrothermal [15], and electromagnetic [16], [17]. Pneumatic systems are fast and contactless but require constant energy input to hold a position, high pressures, complex fluid models and control to predict and control their behavior and are not simple to integrate due to their pipework. Electrostatic systems have high displacement forces, scalability advantages and are easily manufactured with microfabrication techniques, but require high voltages, produce short strokes and present their characteristic "pull-in" failure. Piezoelectric stick-slip systems can achieve long range motions with submicrometer accuracy and high speeds but need high working voltages, are sensible to temperature, present strong nonlinearities such as hysteresis and creep in their displacement. Electrothermal systems generate large strokes and deflections with important forces but have slow response times and consume more power than other actuation principles. Electromagnetic systems: present large strokes with medium forces compared to the other actuation principles; slower response times than piezoelectric or electrostatic actuators but faster than electrothermal actuators; are relatively easy to build and assembly; could generate levitation and driving forces but do not scale as well as the other systems beyond the millimeter size.

This article seeks to harvest the advantages of the electromagnetic and digital actuation principles. This article presents the modeling and validation of a modular and scalable 2×2 array of digital electromagnetic actuators used as a planar microconveyor for rigid objects. We first present the working principles of the system, from the elementary digital actuator to the digital actuator array and its conveyance principle. We then develop a dynamic model used to predict the acceleration, speed, and displacement (kinematics) of the array mobile parts and conveyed object. This developed dynamic model is confronted with previously reported characterization data [18] and newly presented experimental measurements to validate it. The materials and conditions of these experiments are presented and, finally, the specific experimental methods for each test and its results are analyzed and discussed.

II. Principle of the Conveyance System

A. Principle of the Elementary Digital Actuator

The elementary digital actuator is composed of five gold-coated NdFeB permanent magnets in a silicon structure (see Fig. 1). The mobile permanent magnet at the center of the digital actuator is called mobile magnet, with dimensions of $2 \times 2 \times 1.2$ mm^3. The mobile magnet lies in a square cavity of dimensions $2.2 \times 2.2 \times 1$ mm^3, i.e., slightly larger than the mobile magnet cross section. The stroke of the digital actuator in both x and y directions is defined by the gap between the mobile magnet and the cavity (0.2 mm). The other four permanent magnets, named fixed magnets, are fixed around the square cavity. The magnetization of the mobile magnet and fixed magnets are directed along the z-axis in opposite directions to obtain an attracting magnetic force between them. This configuration creates four equilibrium positions for the mobile magnet—each corner of the cavity where the mobile magnet contacts the cavity' walls, giving a digital actuation nature to the elementary digital actuator.

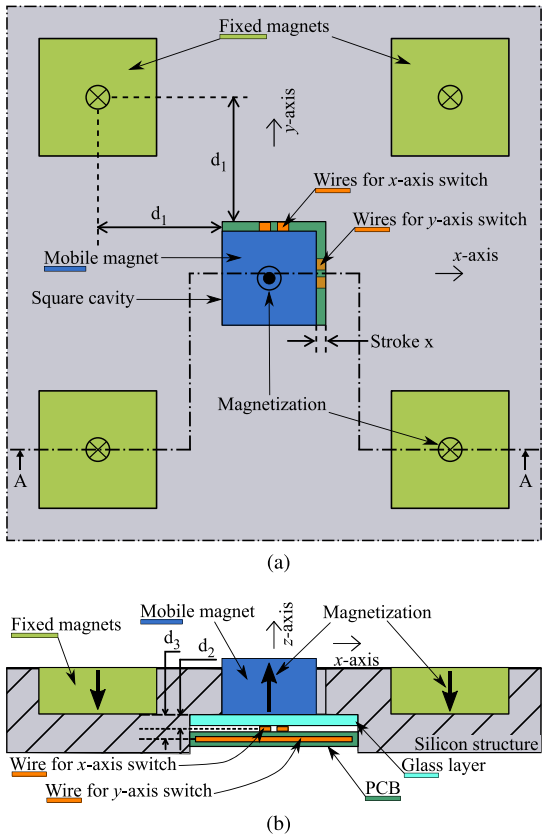

Fig. 1. Elementary digital actuator views (a) top and (b) front (A-A cut).

To actuate the digital actuator, a pair of wires is placed under the cavity for each displacement axis. We chose a pair of wires per axis to maximize the generated electromagnetic force. When an electrical current passes through the wires, a Lorentz force appears between the mobile magnet and the wires. The wires placed along the x-axis switch the mobile magnet in the y-axis and vice versa. We name the wires by its actuating axis, i.e., the x wires are the ones actuating the mobile magnet in the x-axis as shown Fig. 1. The current used to generate a displacement is named *driving current* (I_d). To avoid electrical contact between the two orthogonal pair of wires they are placed in different layers of a 100 μm multilayer printed circuit board. This circuit layer distance was chosen as small as possible to obtain a similar behavior for each axis (d_3). Finally, a thin glass layer is placed between the mobile magnet and the circuit board to avoid their direct contact and give the mobile magnet a plane surface to slide between the discrete positions.

The elementary digital actuator characteristics are presented in Table I. The design parameters d_2, stroke and d_1 were determined, thanks to the developed dynamic model (Section III). d_2 influences the generated electromagnetic force of the driving current and the mobile magnet. We want to maximize this force, thus minimize d_2. For this, a 100 μm glass layer between the mobile magnet and the circuit board is used. Next, we want the stroke to be large to exploit the Lorentz principle of actuation, but

TABLE I
ELEMENTARY DIGITAL ACTUATOR CHARACTERISTICS

Element	Dimensions (mm)	Mass	Material	Mag. (T)
Mobile magnet	2.0 × 2.0 × 1.2	34 mg	NdFeB	1.22
Fixed magnet	2.2 × 2.2 × 1.0	45 mg	NdFeB	1.43
Structure	9.9 × 9.9 × 2.0	104 g	Silicon	–
Glass layer	4.0 × 4.0 × 0.1	64 mg	Glass	–
Object	20 × 20 × 0.1	211 mg	Glass	–

Variable	Distance between	Value (µm)
d_1	Cavity and fixed magnets	2600
d_2	Mobile magnet and x wire	185
Stroke	Stroke in both axes	200
d_3	Mobile magnet and y wire (wire separation)	253
d_4	Mobile and fixed magnets thickness (z-axis)	200

it needs to be short to keep the displacement resolution fine, avoid undesired mobile magnet rotations and keep a compact design. A 200 μm-stroke was chosen as a compromise. To determine d_1, we used the dynamic model (explained in detail in the next section) to calculate the magnetic force on the mobile magnet at its discrete positions (without a conveyed mass). To ensure the digital nature of the actuator, we need this magnetic "holding force" to be as strong as possible, but, a too strong magnetic force would impose a high driving current to overcome the magnetic force and actuate the magnet. A compromise must be found. We chose d_1 to ensure that the mobile magnet will return to its discrete position even if it is at 15% of the stroke value from a discrete position (30 μm for a 200 μm stroke). Finally, to ensure that the mobile magnets are the only contact point with the rigid conveyed object they are thicker than the fixed magnets along the z-axis by 0.2 mm (d_4).

B. Principle of the Digital Actuator Array

The digital actuator array consists of a matrix of elementary digital actuators. Adjacent actuators share a pair of fixed magnets to decrease the array size (a). The array combines individual actions of each actuator to obtain complex tasks, e.g., planar conveyance motions. The "stick-slip" strategy to convey an object on top of the array, using this collaborative actuation, is presented in Fig. 3. The conveyed object is placed on top of the mobile magnets [see Fig. 3(a)]. The mobile magnets are switched simultaneously to displace the object [see Fig. 3(b)]. During this step, the friction force between the mobile magnets and the conveyed object accelerates the object until the mobile magnets reach their discrete position. Once the mobile magnets stop, the dynamic friction due to the relative movement between the moving object and the static mobile magnets acts as a brake to the object until it stops, reaching a "displacement step." The second phase "slip" resets the configuration for a new displacement step: each mobile magnet is individually switched back to return to its initial position [see Fig. 3(c) and (d)]. The friction force between a single mobile magnet and the object is lower than the opposition force of all the other mobile magnets. During the steps represented in Fig. 3(c) and (d), the mobile

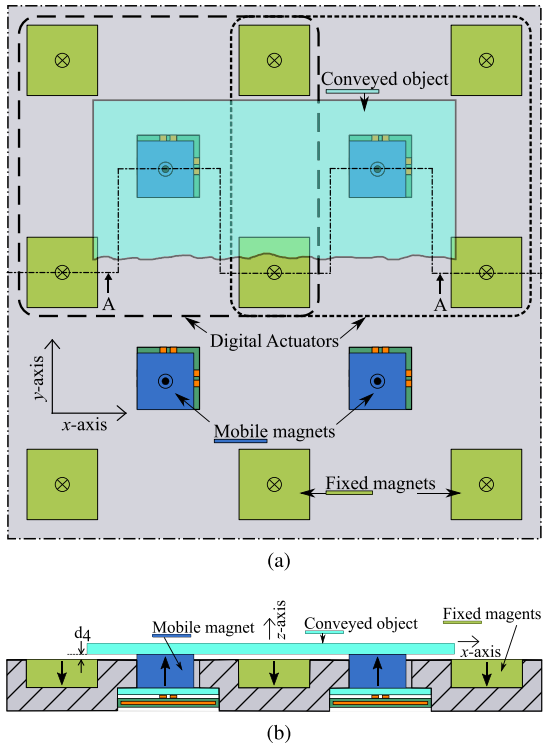

Fig. 2. 2 × 2 digital actuator array views. (a) Top. (b) Front (A-A cut).

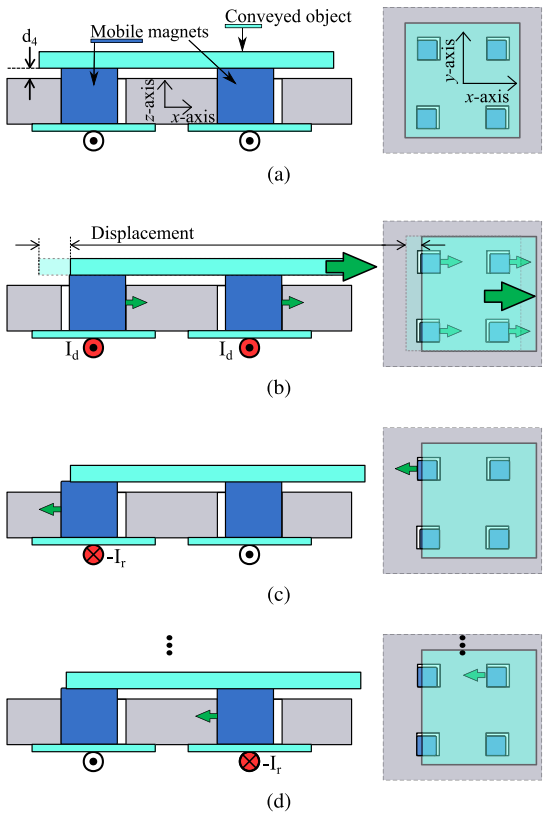

Fig. 3. Side and top views (left and right, respectively) of the stick-slip conveyance principle of the array (one displacement step represented). (a) Initial state. (b) Simultaneous mobile magnet displacement. (c) and (d) Return of the mobile magnets to the initial position.

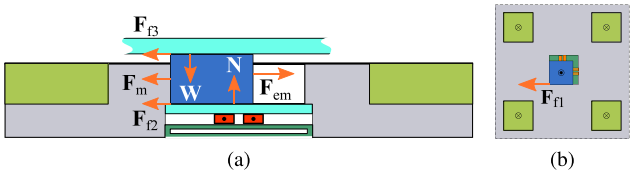

Fig. 4. Free body diagram of the actuator. (a) Front view and (b) top view.

magnet slide without moving the object. When all the mobile magnets are back to the initial position, a new displacement step can begin [see Fig. 3(a)]. The current used to return the mobile magnets to the initial position is noted as return current (I_r) in Fig. 3.

III. Dynamic Model

A dynamic model of the array was developed to predict the acceleration, speed and displacement (kinematic behavior) of the mobile magnets and conveyed object. The model calculates the mobile magnet and conveyed object kinematics as a function of the system variables: intensity and duration of the currents in both actuation axes. Three different types of forces act onto the system: magnetic forces due to the interaction between the permanent magnets, electromagnetic forces due to the interaction between the mobile magnets and the control currents and friction forces between the mobile and fixed parts (see Fig. 4). Each force is calculated at each time-fixed simulation step, as well as the total force acting on the mobile magnet. We estimate the mobile magnet acceleration at each simulation step using Newton's second law and integrate it to obtain its speed and position. We present hereafter the force analysis of the system and then the model of collisions and rebounds of the mobile magnet as it reaches its discrete position.

A. Magnetic Forces Modeling

Equation 1 is used to calculate the magnetic force ($\vec{F}_m$) exerted on the mobile magnet due to the external magnetic flux density generated by the fixed magnets ($\vec{B}_{\text{ext}}$). As explained in [19, Sec. 3.4], this equation is the discrete form of the analytical solution as it is not always possible to implement the analytical expression, so we divide the mobile magnet poles surface S into p areas ΔA

$$\vec{F}_m = \sum_p \sigma_m(\vec{x}_p)\vec{B}_{\text{ext}}(\vec{x}_p)\Delta A_{p'} \tag{1}$$

where σ_m is the "magnetic surface charge density" of the mobile magnet, $\vec{B}_{\text{ext}}$ is the total external magnetic flux density generated by the fixed magnets on each area element ΔA, and $\vec{x}_p$ is the relative position vector of each area element. $\vec{B}_{\text{ext}}$ is derived from the charge model considering each fixed magnet as a perfect square prism and with their magnetization vector perfectly aligned along the z-axis ($\vec{M} = M\vec{z}$, see Mag. in Table I). The Cartesian coordinates components of one fixed magnet $\vec{B}_{\text{ext}}$ are presented

$$B_x(x,y,z) = \frac{\mu_0 M}{4\pi}\sum_{k=1}^{2}\sum_{m=1}^{2}(-1)^{k+m} \times \ln\left[\frac{(y-y_1)+\sqrt{(x-x_m)^2+(y-y_1)^2+(z-z_k)^2}}{(y-y_2)+\sqrt{(x-x_m)^2+(y-y_2)^2+(z-z_k)^2}}\right] \tag{2}$$

$$B_y(x,y,z) = \frac{\mu_0 M}{4\pi}\sum_{k=1}^{2}\sum_{m=1}^{2}(-1)^{k+m} \times \ln\left[\frac{(x-x_1)+\sqrt{(x-x_1)^2+(y-y_m)^2+(z-z_k)^2}}{(x-x_2)+\sqrt{(x-x_2)^2+(y-y_m)^2+(z-z_k)^2}}\right] \tag{3}$$

$$B_z(x,y,z) = \frac{\mu_0 M}{4\pi}\sum_{k=1}^{2}\sum_{n=1}^{2}\sum_{m=1}^{2}(-1)^{k+m+n} \times \tan^{-1}\left[\frac{(x-x_n)(y-y_m)}{(z-z_k)\sqrt{(x-x_n)^2+(y-y_m)^2+(z-z_k)^2}}\right] \tag{4}$$

where $(x_2-x_1),(y_2-y_1),(z_2-z_1)$ are the fixed magnet dimensions, and M is the fixed magnet magnetization [19].

B. Electromagnetic Force Modeling

To model the force exerted on the mobile magnet by the current-carrying wires beneath it, we use (5). With I the current injected in the wire, $\mathrm{d}\vec{l}$ the vector along the wire length, and $\vec{B}_{\text{ext}}$ the magnetic flux density generated by the mobile magnet [19]

$$\vec{F_{\text{em}}} = I\int_{wire}\mathrm{d}\vec{l}\times\vec{B}_{\text{ext}} \tag{5}$$

C. Friction Modeling

The conveyance task obtained with the array is based on a "stick-slip" frictional principle. We modeled the friction phenomena between the mobile magnet, the silicon cavity walls, the glass support, and the conveyed object ($\vec{F}_{\text{f1}}$, $\vec{F}_{\text{f2}}$, and $\vec{F}_{\text{f3}}$ in Fig. 4), adapting the work of Bengisu and Akay [20] (6). Their model captures the Stribeck effect that was experimentally observed in our system [18], [21]

$$\vec{F}_{\text{f}} = \begin{cases} \left(-\frac{F_s}{v_0^2}\left(\|v\|-v_0\right)^2+F_s\right)s\vec{g}n(v) & \|v\|<v_0 \\ \left(F_c+(F_s-F_c)e^{-\zeta(\|v\|-v_0)}\right)s\vec{g}n(v) & \|v\|>v_0 \end{cases} \tag{6}$$

where v is the speed of the mobile magnet, F_s is the value of static friction, F_c is the value of the settling friction when v tends to ∞, v_0 is the transition speed value between the static friction and dynamic friction, and ζ is the decay factor for the dynamic friction [20]. We determined the friction model parameters with a separate energy-based set of experiments and a root mean square error identification process, obtaining the results presented in (Table II).

TABLE II
PARAMETERS OF THE DYNAMIC MODEL AND CHARACTERISTIC VALUES OF THE ELEMENTARY DIGITAL ACTUATOR

Symbol	Variable/Conditions	Value	Unit
$\vec{F}_{\mathrm{m}}$	Magnetic force at a discrete position	0.43	mN
l	Length of the wires	8.00	mm
$\vec{F}_{\mathrm{emx}}$	x-axis electromagnetic force at cavity's center	1.22	mN/A
$\vec{F}_{\mathrm{emy}}$	y-axis electromagnetic force at cavity's center	1.05	mN/A
μ_s	Static friction coefficient	1.00	-
μ_c	Dynamic friction coefficient	0.80	-
v_0	Transition speed	93.0	mm s^{-1}
ζ	Decay factor	300	s mm^{-1}
$\vec{F}_{\mathrm{f1}}$	Friction force magnet-silicon at 50 mm s^{-1}	0.11	mN
$\vec{F}_{\mathrm{f2,f3}}$	Friction force magnet-glass at 50 mm s^{-1}	0.50	mN
Y	Yield pressure	165	MPa
E	Equivalent Young modulus	35.7	GPa
ρ	Mobile magnet Density	7.01	g cm^{-3}
m_a	Mobile magnet mass	34.0	mg
m_b	Silicon structure mass	104	g
C_{R}	Coeff. of restitution at 0.8 m s^{-1}	0.78	-

D. Collision and Rebound Effect Modeling

Because of the digital principle of the system, the mobile magnet impacts the cavity walls when arriving to its discrete positions. The collision and rebound of the mobile magnet due to this impact were modeled implementing the classic equations of elasto-plastic collisions in one dimension [22]

$$v_a = \frac{m_{\mathrm{a}}u_{\mathrm{a}} + m_{\mathrm{b}}u_{\mathrm{b}} + m_{\mathrm{b}}C_{\mathrm{R}}\left(u_{\mathrm{b}} - u_{\mathrm{a}}\right)}{m_{\mathrm{a}} + m_{\mathrm{b}}} \tag{7}$$

$$v_b = \frac{m_{\mathrm{a}}u_{\mathrm{a}} + m_{\mathrm{b}}u_{\mathrm{b}} + m_{\mathrm{a}}C_{\mathrm{R}}\left(u_{\mathrm{a}} - u_{\mathrm{b}}\right)}{m_{\mathrm{a}} + m_{\mathrm{b}}} \tag{8}$$

where v_{a} and u_{a} are the speed of the mobile magnet after and before collision, respectively. v_{b} and u_{b} are the speed of the structure after and before collision, respectively. m_{a} and m_{a} are the mass of the mobile magnet and structure, respectively. We suppose that the structure is static before and after the collision ($v_{\mathrm{b}} = u_{\mathrm{b}} = 0$) given its large mass compared to the one of the mobile magnet ($m_{\mathrm{b}} \gg m_{\mathrm{a}}$). C_{R} is the restitution coefficient for the collision between the mobile magnet and the structure. We model this coefficient following the work of Weir and Tallon [23]. If we consider that the cavity wall and mobile magnet side surfaces are plane, their equation of C_{R} is given by

$$C_{\mathrm{R}} = \alpha \left(\frac{Y}{1}\right)^{\frac{5}{8}} \left(\frac{1}{E}\right)^{\frac{1}{2}} \left(\frac{1}{v}\right)^{\frac{1}{4}} \left(\frac{1}{\rho}\right)^{\frac{1}{8}} \tag{9}$$

where Y is the yield pressure, E is the equivalent Young modulus between neodynium and silicon, ρ is the density of the mobile magnet material (in our case neodymium), and v is the mobile magnet impact speed. α, a numerical coefficient dependent of the colliding particles' geometry, hardness and contact area, is taken as 1 [23].

Finally, Newton's second law is used to compute the total force onto the mobile magnet and the energy transferred to the conveyed object by friction. Results of the dynamic model compared to experimental measures are presented in Section V.

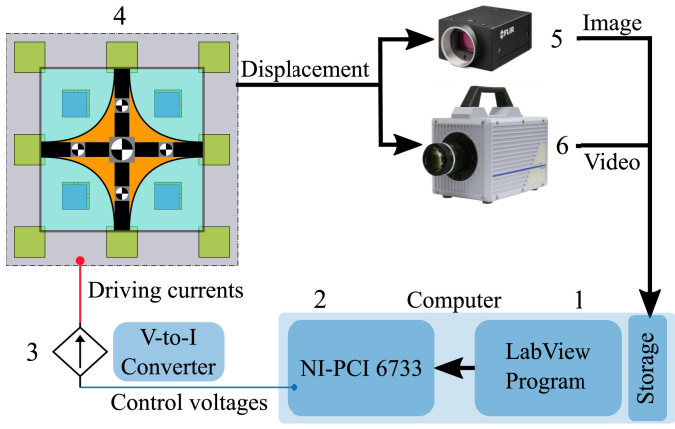

(a)

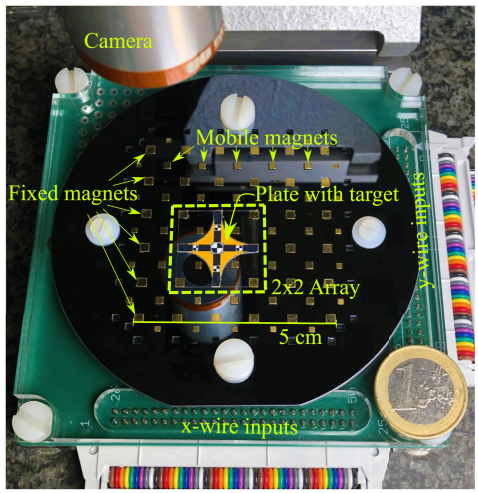

(b)

Fig. 5. (a) Control scheme of the 2 × 2 digital actuator array: 1. Computer with Labview interface. 2. National Instruments PCI6733 DAQ. 3. Multiple voltage-controlled current sources. 4. The 2 × 2 array system. 5. Grasshopper3 GS3-U3-32S4C camera. 6. Photron FastCam SA1.1 camera. (b) Picture of the real implementation and components in a 5 × 5 digital actuator array.

IV. MATERIALS

The material and signal flux involved in all the experimental set ups are schematized in Fig. 5(a). The system is controlled with a developed LabVIEW interface [see Fig. 5 a(1)], connected to a National Instruments PCI6733 input/output board [see Fig. 5 a(2)] that sends four control voltages (+10 V) to four current sources, producing a maximal output of +10 A each [see Fig. 5 a(3)]. The four current signals are injected in the actuators wires [see Fig. 5 a(4)]. The displacement and dynamics of the conveyed object and mobile magnets are measured using two cameras placed on top of the array. To measure the displacement of the object (a static measure once the displacement step is done), we use a Grasshopper3 GS3-U3-32S4C with a fixed optic system providing an image with a 0.694 μm/pixel resolution [see Fig. 5 a(5)]. The kinematics of the mobile magnet and

object (a dynamic measure of displacement through time) are measured with a Photron FastCam SA1.1 camera at 15 000 Hz with a variable optic system providing images with resolutions between 2.45 and 16.1 μm/pixel [see Fig. 5 a(6)]. Fig. 5(b) shows a picture of the real system. The conveyed object was a glass plate with a sticker target. The object weight was 211 +1 mg and had a size of 20 × 20 × 0.1 mm. We measured each experimental point 20 times to obtain a mean value as well as a standard deviation, represented by the error bars in the figures ahead.

V. Methods, Results, and Discussion

This section presents the comparison between the developed dynamic model and the experimental measurements of the presented prototype. We first present the kinematics of the mobile magnets and the conveyed object. Second, the influence of the current intensity on the conveyed object displacement. Third, the influence of the current pulse width on the conveyed object displacement and, finally, bidimensional displacements of the conveyed object by simultaneous activation of the two axis of the digital actuators.

A. Mobile Magnet and Conveyed Object Kinematics Along One Axis

We studied the kinematic behavior (displacement versus time) of the mobile magnets and the conveyed object at different current intensities and along one axis. We injected a driving current into the x-axis wires for 100 ms to ensure that the pulse was longer than the response time of the system. We varied the pulse intensity to evaluate its influence on the kinematics of the system. Fig. 6 presents a comparison between the dynamic model and experimental results. Fig. 6(a) shows the kinematics of the mobile magnet and the conveyed object under a 5 A driving current. Fig. 6(b) and (c) show the influence of the current intensity on the mobile magnet and object kinematics, respectively.

From Fig. 6(a), we observed that, as the mobile magnet moves forward, it transferred energy to the object by friction, dragging the object forward with it. As the mobile magnet reached the stroke distance of 200 μm, it rebounded, generating an opposing friction force on the conveyed object. The result was an inflection point in the object displacement curve. The dynamic model predicts that, after the first rebound, the electromagnetic and magnetic forces drive the mobile magnet toward the desired discrete position. This causes a second rebound with a smaller amplitude. This rebound process repeated until the mobile magnet rested in the discrete position. When the mobile magnet finally stayed stationary, the remaining kinetic energy of the object was dispersed by friction until the object stopped. This cycle represents one displacement step as explained in Fig. 3.

From Fig. 6(b), we observed that the final mobile magnet displacement value was independent of the current intensity, demonstrating the digital nature of its actuation principle. This displacement value was 200 μm. The settling and rise time of the mobile magnet varied with the value of current intensity: as the current intensity increased the kinematics of the mobile magnet were faster, shortening both the rise time and the settling time. We defined the rise time as the time needed for the output to reach from 10% to 90% of its final value. We measured mobile magnet rising times between 0.8 and 3 ms.

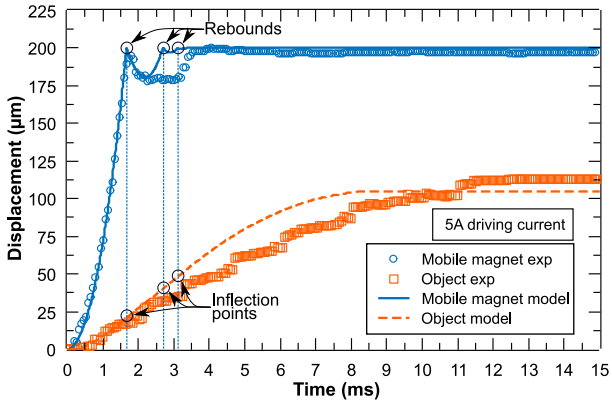

(a)

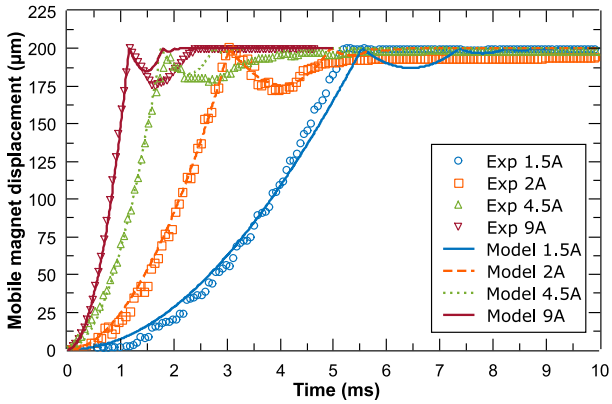

(b)

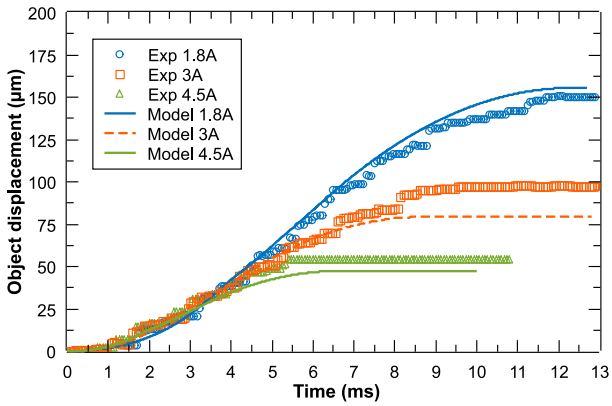

(c)

Fig. 6. Experimental and modeled kinematics of (a) mobile magnet and conveyed object for a 5 A driving current, (b) mobile magnet kinematics for different driving current intensities, and (c) conveyed object kinematics for different driving current intensities.

From Fig. 6(c), we observed a final object displacement value that varied with the current intensity (between 50 and 150 μm). This displacement range was due to the fact that the object is carried by the mobile magnets and then slides on top of them with different kinetic energies for different speeds of the mobile magnets (6). We measured rising times of the conveyed object between 3.7 and 7.5 ms.

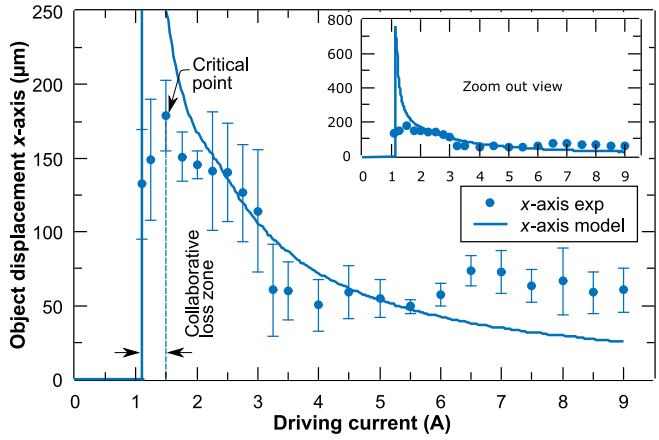

(a)

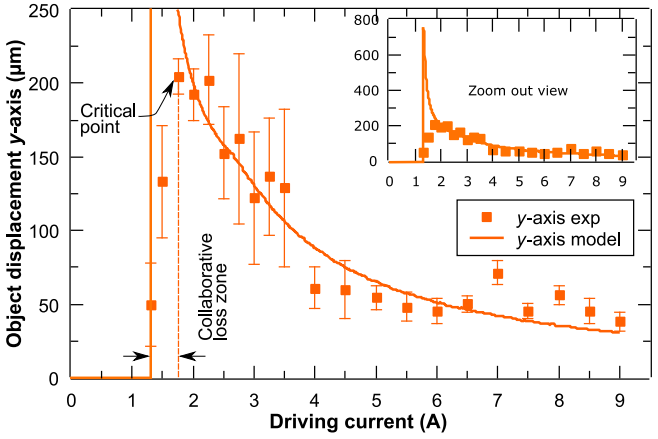

(b)

Fig. 7. Conveyed object displacement versus driving current intensity in the (a) *x*-axis and (b) *y*-axis.

From Fig. 6, we observed that the model predicted the kinematics of the mobile magnet and conveyed object in both the rising part of the curve, the rebound phenomena, and the settling value. We calculated the root-mean-square error (RMSE) between the dynamic model and all the experimental measures presented in Fig. 6. For the mobile magnet tests, the mean RMSE ($\pm$ std) was $5.72 + 0.89$ μm (which corresponds to 2.9 % of the actuator stroke). For the conveyed object tests, the mean RMSE was $7.38 + 3.32$ μm (which corresponds to 3.7 % of the actuator stroke).

B. Linear Motion of the Object Along One Axis

To validate the dynamic model as a prediction tool for the conveyance system, we studied the influence of the current intensity and pulse duration on the conveyed object displacement step along each axis separately.

1) Influence of the Driving Current Intensity: We injected a driving current in only one of the two pair of wires of each actuator at a time to obtain a linear motion of the mobile magnet and the object along that axis only. The same pulse duration used in Section V-A (100 ms) was selected. Fig. 7 presents the displacement of the conveyed object as a function of the driving current intensity for both the *x*- and *y*-axes.

From Fig. 7, we observed that the object displacement decreased as the current increased. The higher the injected current, the faster the mobile magnet kinematics, reducing the displacement time and energy transfer through friction to the object. The model predicted this tendency correctly. The error bars decreased as the driving current increased. This is attributed to the important influence of the friction conditions at lower currents and its reduced influence with faster kinematics as the current increases.

We observed a maximum experimental displacement at (1.5 A, 179.3 μm) for the *x*-axis and (1.75 A, 204.5 μm) for the *y*-axis. At these points, the energy transferred to the plate through friction was maximized though a slow mobile magnet movement that prevents slipping phenomena of the actuation. We call these points "critical points" in Fig. 7. The value of the critical point along the *y*-axis was higher than along the *x*-axis. This is explained by the difference in distance between the currents wires and the mobile magnet (d_2 and d_3 in Fig. 1). The model predicted greater displacements with lower currents than 1.5 or 1.75 A, but experimentally, we observed another phenomenon: the displacement decreased sharply as the collaborative effect of the array was lost due to the heterogeneous nature of friction. This zone of displacement collapse is called the "collaborative loss zone" in Fig. 7. This collaborative loss zone was not predicted by the model as it considers all actuators perfectly homogeneous.

Inside the collaborative loss zone, we observed that the experimental displacements of the object started from current values of 1.1 A for the *x*-axis and 1.5 A for *y*-axis, in accordance with the model. Lower current values did not generate enough electromagnetic forces to overcome the magnetic holding and friction forces of the mobile magnet and object. The RMSE between the model and the experimental values were 29.87 μm for the *x*-axis and 19.05 μm for the *y*-axis (without considering the collaborative loss zone).

We measured the straightness error of all the experimental points of Fig. 7. We explain this error by the asynchronous movement of the mobile magnets due to the heterogeneity in friction, causing a torque to appear. Also, manufacturing and assembly errors like the misalignment between the wires and the actuators' axes could contribute to this error. The mean straightness error for all current values were $13.3 + 6.8$ μm for the *x*-axis and $10.5 + 5.4$ μm for the *y*-axis.

To finish this section, we focus on the driving currents from 5 to 9 A in Fig. 7. Under these conditions, the influence of the different initial conditions of the mobile magnets such as position and friction heterogeneity are reduced against the rapid dynamic of the system, explaining the smaller error bars on Fig. 7 for both axes. This high current zone is then useful for repeatable and precise object displacement steps. The average error bar was 11 μm for the *x*-axis and 7.5 μm for the *y*-axis. The average straightness error was 11 μm for the *x*-axis and 6.2 μm for the *y*-axis. The minimum error bar was 4.7 μm for the *x*-axis and 5.3 μm for the *y*-axis. The straightness errors of these last two points were 5.2 and 3.9 μm, respectively.

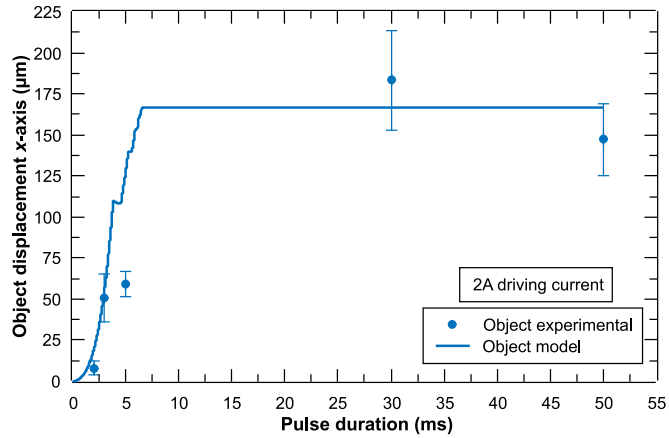

(a)

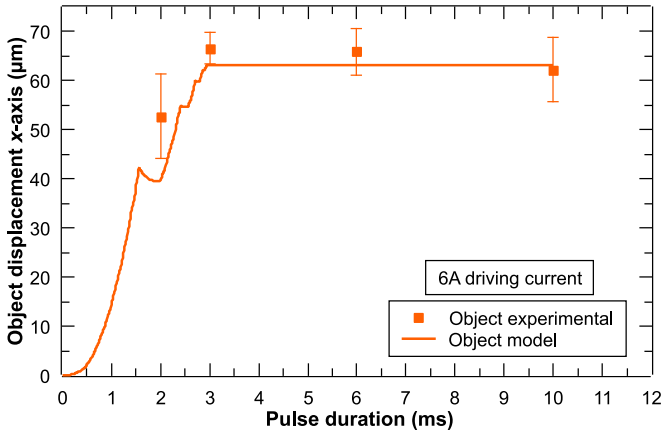

(b)

Fig. 8. Conveyed object displacement versus driving current pulse duration for (a) 2 A along the *x*-axis and (b) 6 A along the *x*-axis.

2) Influence of the Driving Current Pulse Duration: We injected a driving current pulse along the *x*-axis only. We varied the pulse duration to observe its influence on the displacement step of the conveyed object. Fig. 8 presents the displacement step value as a function of the driving current pulse duration for current intensities of 2 A [Fig. 8(a)] and 6 A [Fig. 8(b)]. From Fig. 8, we observed a similar behavior for the two driving current intensities—the model predicted an increasing object displacement as the pulse duration increased until a saturated displacement value. When the pulse duration was longer than the whole kinematics of the mobile magnets, including all rebounds, the pulse duration no longer influenced the object's displacement, explaining this saturation. Before this saturated value, the effect of the rebound of the mobile magnets on the object displacement were visible [notably on Fig. 8(b)]. The model predicted the experimental measures with an RMSE of 14.2 μm for the 2 A test and 6.86 μm for the 6 A test.

C. Bidimensional Linear Motion of the Object

We injected a current into both wires beneath each actuator to obtain an object displacement in both *x* and *y* axes ("I_x" and "I_y,"

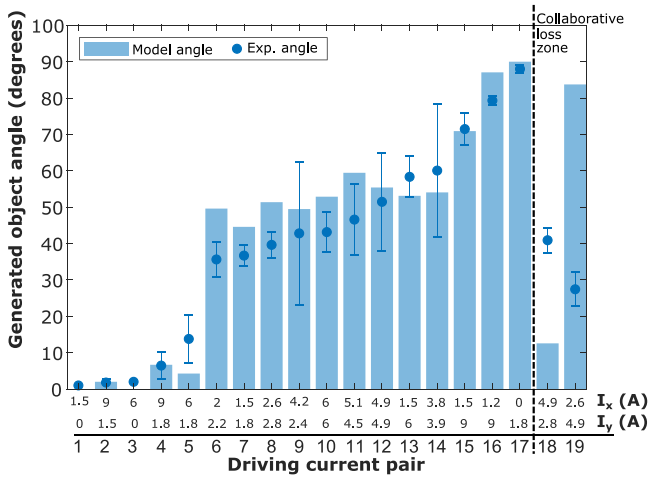

Fig. 9. Predicted and experimental object angle (in degrees) for different (I_y, I_x) pairs.

respectively). Each combination of I_x and I_y is called a current pair. We measured the angle of this bidimensional movement to the *x*-axis for multiple currents pairs. The pulse duration of the current pairs were larger than the kinematics of the mobile magnets as in Section V-A. The bar plot in Fig. 9 presents the experimental and model-predicted angle as a function of the injected currents pairs. Each current pair identification number is presented in the lower horizontal axis of Fig. 9. The experimental value is the mean of 20 measures per point with its standard deviation represented as error bars.

When one of the driving current was zero ($I_x = 0$ or $I_y = 0$), we obtained a 1-D linear displacement along the correspondent axis, i.e., an angle tending to 0° along $I_y = 0$ and 90° along $I_x = 0$ (pairs 1, 3, and 17 in Fig. 9). For similar values of I_x and I_y, we obtained similar displacements on both axes, i.e, angles tending to 45° (experimentally from 43.16° to 51.48° for pairs 10–12 in Fig. 9).

For opposing magnitudes of I_x and I_y currents we observed an antagonistic phenomena: as shown in Fig. 7, a low current generated a big displacement of the object, so the low current axis should generate a big displacement. On the other hand, the mobile magnet moved quicker in the high current axis than in the low current axis. As the mobile magnet arrived to its stroke in the high current axis it contacted the wall's cavity, creating a friction force. The high current along such axis increased the mentioned friction force opposing and limiting the displacement along the low current axis. The dynamic model predicted the experimental results with a root mean squared error of 6.82° (excluding the collaborative loss points). The mean standard deviation for all the experimental points (angle repeatability, error bars) was 6.3°.

Lastly, we discuss the pairs 18 and 19 of Fig. 9. On those points we observed the antagonistic phenomena described before, but the current difference between the currents was small (2.07 and 2.31 A, respectively). With this smaller current difference, as the mobile magnet arrived to the stroke distance, the created friction force was not as overwhelming as the previous explained antagonistic phenomena and the system entered the "collaborative

TABLE III
LITERATURE COMPARISON

	Scalable	DoF	Active Surface	Actuator	Control	Conveyed object	Speed	Precision/Error
[3]	No	1	⌀30 cm	Analog	Closed	30 mm × 30 mm	-	12.5 µm
[4]	Yes	16	93 mm × 110 mm	Analog	Closed	-	7 mm s^{-1}	-
[5]	Yes	3	300 mm × 225 mm	Analog	Closed	⌀150 mm	300 mm s^{-1}	25-230 µm
[6]	Yes	3	9 mm × 9 mm	Analog	Open	3 mm, 2 mg	2-3 mm s^{-1}	-
[7], [8]	Yes	3	120 mm × 120 mm	Analog	Closed	30 mm × 15 mm, 3.3 g	167 mm s^{-1}	0.242 mm - 2.5 mm
[9]	Yes	2	645 mm^2	Analog	Closed	5 mm × 5 mm, 2.1 g	-	350-550 µm
[10]	Yes	2	750 mm × 170 mm	Analog	Open	90 mm × 100 mm, 139 g	50 mm s^{-1}	-
[11]	Yes	2	290 mm × 290 mm	Analog	Open	132 mm × 132 mm, 11 g	250 mm s^{-1}	400 µm
[12]	Yes	6	1.1 mm × 1.1 mm	Analog	Closed	150 µm × 100 µm × 50 µm, 0.9 µg	1.5 rad s^{-1}	-
[13]	No	1	-	Analog	Open	260 mg	123 rad s^{-1}	-
[14]	No	3	±5 mm, 90°	Analog	Closed	⌀300 mm, 129 g	< 2 mm s^{-1}	0.4 mm
[15]	Yes	3	40 mm × 40 mm	Digital	Closed	7 mm × 5 mm	0.67 mm s^{-1}	2-22 µm
[16]	Yes	3	150 mm × 150 mm	Analog	Closed	68 mm × 68 mm, 3.6 g	12 mm s^{-1}	pos 7 µm, straig 65 µm
[17]	No	2-6	5 mm × 5 mm	Analog	Closed	6.5 kg	-	32 µm-45 µm
Present	Yes	3	100 mm × 100 mm	Digital	Open	20 mm × 20 mm, 211 mg	2 mm s^{-1}	pos 4.7 µm straig. 5.2 µm

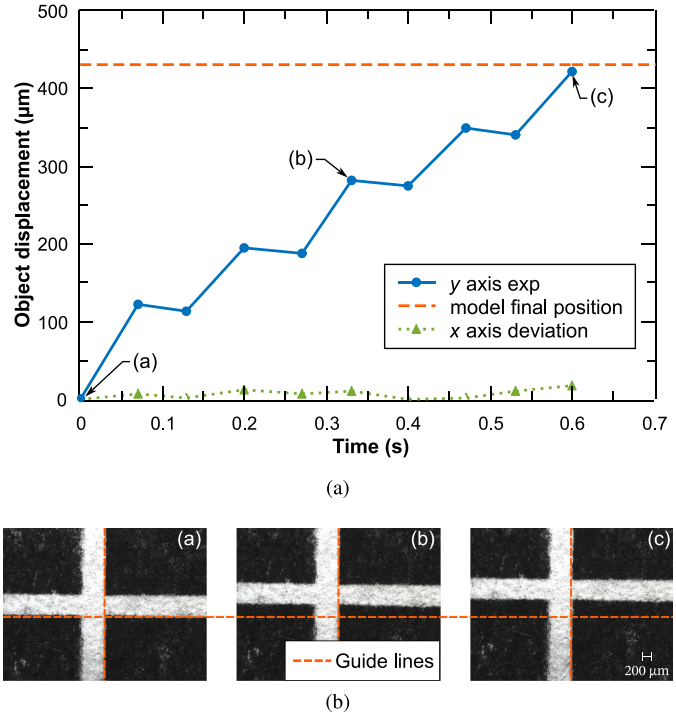

Fig. 10. (a) Object trajectory for five displacement steps in the *y*-axis. (b) Correspondent object photos at given time.

loss zone" explained before (Section V-B1). This explains the divergence between the model and the experimental results on these points.

D. MultiStep Linear Motion

We repeated the conveyance strategy presented in Fig. 3 along the *y*-axis for 5 times with a driving current (I_d) of 3.5 A during 100 ms and a return current (I_r) of 7 A for 20 ms. Fig. 10 presents the obtained trajectory of the conveyed object along the *y*-axis after five displacement steps and the straightness error (*x*-axis displacement), as well as the model-predicted total displacement of the object.

From Fig. 10(a), we measured a mean experimental displacement per step of 90.92 μm and a total displacement of 422.72 μm. The predicted displacement per step was 86.15 μm and total displacement of 430.76 μm (model position error of 4.77 μm per step, 8 μm final position). The total straightness error was 8.18 μm. The observed straightness error did not propagate with multiple step displacement and could be corrected with an additional displacement step after the desired conveyance task. Through all the presented experimental results, we observed no accidental rotation of the conveyed object. An unexpected displacement due to the return current was observed in the actuated axis. The average return displacement was 7.97 μm.

E. Performance Comparison With Literature Systems

The requirements for a microconveyor could vary depending on the architecture, machining stations, and geometry of the factory where it is implemented. Some common requirements are the largest possible active area, with planar motion capabilities [three-degrees-of-freedom (3-DoF)], speeds up to millimeters per second and the smallest position error possible, as well as minimizing its energy consumption. Then, depending on the conveyed object size, shape, and weight, additional requirements need to be added. As discussed in Section I, the integration of this conveyor should be easy, keeping the complexity of the whole factory as low as possible, thus the importance of the control structure and its interaction with the machining/measuring stations. Table III presents a comparison of proposed solutions in the literature for microconveyance and the performance of our system relative to them. Following the comparison of Table III and the performance presented in this article, our system strengths are the mentioned digital actuation principle and simple control, the modular and scalable design of the array, 3-DoF capability, significant active surface to object size relation, competitive speed, position precision, and low

energy consumption. Judging from the presented general requirements and performance relative to other solutions, we state that our solution could find its place among the microconveyance systems for the microfactory, offering the flexibility needed to adapt to the changing architecture of the microfactories.

VI. Conclusion

In this article, we presented a digital actuator array based on a matrix of elementary digital actuators of electromagnetic nature. The proposed application of the array, as stick-slip microconveyance system, was experimentally validated. A dynamic model of the array, considering its magnetic, electromagnetic, friction, collision, and rebound phenomena, was developed and compared to the experimental measurements. The dynamic model correctly predicted the kinematics of the system as well as the unidimensional and bidimensional displacements of the conveyed object with low root-mean-square errors. From the experimental measurements, we obtained digital actuator rising times from 0.8 ms. For the conveyed object, we measured rising times from 3.7 ms. The maximum conveyed object displacement per displacement step was 204.5 μm, and the minimum was 7.9 μm. We obtained unidimensional motion of the conveyed object with a minimum straightness error of 5.2 and 3.88 μm (x-axis and y-axis, respectively) and a position repeatability of 4.7 and 5.3 μm (x-axis and y-axis, respectively). We demonstrated the bidimensional motion capability of the array with a spectrum of conveyed object angles from 1° to 88°.

Future work will be centered in expanding the array active area by assembling multiple arrays together, reducing the needed number of power signals and sources with a dedicated digital control circuit and then evaluating multiple objects conveyed at the same time. The dynamic model will be used to develop model-based control strategies that ensure the trajectory, position, speed, acceleration, and collision avoidance of the conveyed objects as well as optimizing the energy consumption. The dynamic model could be extended to include planar rotation of the conveyed objects to predict complex motions, following the 3-DoF of the array. Finally, the development of a thermal study of the system to find its operational limit is in our perspectives.

References

[1] Y. Okazaki, N. Mishima, and K. Ashida, "Microfactory—concept, history, and developments," *J. Manuf. Sci. Eng.*, vol. 126, no. 4, pp. 837–844, 2004.

[2] D. Gendreau, M. Gauthier, D. Hériban, and P. Lutz, "Modular architecture of the microfactories for automatic micro-assembly," *Robot. Comput.-Integr. Manuf.*, vol. 26, no. 4, pp. 354–360, 2010.

[3] Z. Zhakypov, T. Uzunovic, A. O. Nergiz, E. A. Baran, E. Golubovic, and A. Sabanovic, "Modular and reconfigurable desktop microfactory for high precision manufacturing," *Int. J. Advanced Manuf. Technol.*, vol. 90, pp. 3749–3759, 2017.

[4] M. A. Robertson, M. Murakami, W. Felt, and J. Paik, "A Compact modular soft surface with reconfigurable shape and stiffness," *IEEE/ASME Trans. Mechatronics*, vol. 24, no. 1, pp. 16–24, Feb. 2019.

[5] V. Guelpa, G. J. Laurent, B. Dahroug, and N. Le Fort-Piat, "Modular contact-free conveyors for handling planar fragile objects," *IEEE Trans. Robot.*, vol. 33, no. 1, pp. 92–101, Feb. 2017.

[6] R. Zeggari, R. Yahiaoui, J. Malapert, and J. F. Manceau, "Design and fabrication of a new two-dimensional pneumatic micro-conveyor," *Sensors Actuators, A, Physical*, vol. 164, no. 1/2, pp. 125–130, 2010.

[7] A. Delettre, G. J. Laurent, and N. Le Fort-Piat, "A new contactless conveyor system for handling clean and delicate products using induced air flows," in *Proc. IEEE/RSJ Int. Conf. Int. Robots Syst.*, 2010, pp. 2351–2356.

[8] G. J. Laurent, A. Delettre, R. Zeggari, R. Yahiaoui, J. F. Manceau, and N. L. Fort-Piat, "Micropositioning and fast transport using a contactless micro-conveyor," *Micromachines*, vol. 5, no. 1, pp. 66–80, 2014.

[9] E. Yusifli *et al.*, "FPGA-based HD camera system for the micropositioning of biomedical micro-objects using a contactless micro-conveyor," *Micromachines*, vol. 8, no. 3, 2017, Art. no. 74.

[10] K. Furutani, Y. Nakamura, and A. Urita, "Conveyance method of thin plate by using multiple-phase air flow," *Electron. Commun. Jpn.*, vol. 101, no. 2, pp. 51–60, 2018.

[11] T. Hosobata, A. Yamamoto, and T. Higuchi, "Transparent synchronous electrostatic actuator for long-stroke planar motion," *IEEE/ASME Trans. Mechatronics*, vol. 20, no. 4, pp. 1765–1776, Aug. 2015.

[12] T. Michalek, A. Bolopion, Z. Hurak, and M. Gauthier, "Electrorotation of arbitrarily shaped micro-objects: Modeling and experiments," *IEEE/ASME Transactions Mechatronics*, vol. 25, no. 2, pp. 828–836, Apr. 2019.

[13] T. Mashimo, "Micro ultrasonic motor using a cube with a side length of 0.5 mm," *IEEE/ASME Trans. Mechatronics*, vol. 21, no. 2, pp. 1189–1192, Apr. 2016.

[14] R. Gabai, R. Shaham, S. Davis, N. Cohen, and I. Bucher, "A contactless stage based on near-field acoustic levitation for object handling and positioning-concept, design, modeling, and experiments," *IEEE/ASME Trans. Mechatronics*, vol. 24, no. 5, pp. 1954–1963, Oct. 2019.

[15] M. Ataka, B. Legrand, L. Buchaillot, D. Collard, and H. Fujita, "Design, fabrication, and operation of two-dimensional conveyance system with ciliary actuator arrays," *IEEE/ASME Trans. Mechatron.*, vol. 14, no. 1, pp. 119–125, Feb. 2009.

[16] N. Arora, M. U. Khan, L. Petit, F. Lamarque, and C. Prelle, "Design and development of a planar electromagnetic conveyor for the microfactory," *IEEE/ASME Trans. Mechatronics*, vol. 24, no. 4, pp. 1723–1731, Aug. 2019.

[17] H. Zhu, T. J. Teo, and C. K. Pang, "Magnetically levitated parallel actuated dual-stage (Maglev-PAD) system for six-axis precision positioning," *IEEE/ASME Trans. Mechatronics*, vol. 24, no. 4, pp. 1829–1838, Aug. 2019.

[18] S. Duque Tisnés, Z. Shi, L. Petit, C. Prelle, and F. Lamarque, "Characterization of a micro-fabricated digital actuator array as a micro-factory conveyor device," in *Proc. IEEE/ASME Int. Conf. Advanced Intell. Mechatronics.*, 2019, pp. 382–387.

[19] E. P. Furlani, *Permanent Magnet And Electromagnetical Devices*, I. Mayergoyz, Ed., New York, NY, USA: Elsevier, 2001.

[20] M. T. Bengisu and A. Akay, "Stability of friction-induced vibrations in multi-degree-of-freedom systems," *J. Sound Vib.*, vol. 171, no. 4, pp. 557–570, 1994.

[21] F. Marques, P. Flores, J. C. Pimenta Claro, and H. M. Lankarani, "Survey and comparison of several friction force models for dynamic analysis of multibody mechanical systems," *Nonlinear Dyn.*, vol. 86, no. 3, pp. 1407–1443, 2016.

[22] H. Semat and R. Katz, "Momentum and Impulse," in *Physics*. Lincoln, NE, USA: Robert Katz Publications, University of Nebraska-Lincoln, 1958, ch. 10, p. 142.

[23] G. Weir and S. Tallon, "The coefficient of restitution for normal incident, low velocity particle impacts," *Chem. Eng. Sci.*, vol. 60, no. 13, pp. 3637–3647, 2005.

Simón Duque Tisnés received the physics engineer degree from the EAFIT University, Medellin, Colombia, and the M.Sc degree in mechatronics from the Université de Technologie de Compiègne, Compiègne, France, in 2016 (double degree program).

He is currently a Ph.D. Fellow with the Research Team "mechatronics, energy, electricity, and integration" since 2017, working on control strategies and optimization for digital actuators and digital actuator arrays.

Laurent Petit received the Ph.D. degree in mechanical engineering from the Universit de Technologie de Compiègne, Compiègne, France, in 2009.

He is currently an Associate Professor of mechanical and mechatronics engineering with the Roberval Laboratory of Universit de Technologie de Compigne. He is also a Member of the Laboratory of Excellence “Control of Technological Systems-of-Systems (labex MS2T) and is In-Charge of the mechatronics systems master’s degree specialty. His research interests include mechatronic systems, compact electromagnetic actuators, and digital actuation.

Christine Prelle received the Ph.D. degree in industrial automatic control from Institut National des Sciences Appliqueés Lyon, Villeurbanne, France, in 1997.

She is currently a Professor of control engineering and mechatronics with Roberval Laboratory, Université de Technologie de Compiègne, Compiègne, France. She is a Member of the Laboratory of Excellence Control of Technological Systems-of-Systems (labex MS2T). She is currently In-Charge of the Doctoral School Science for Engineers, Université de Technologie de Compiègne, Compiègne, France. Her research interests include micromechatronics and control.

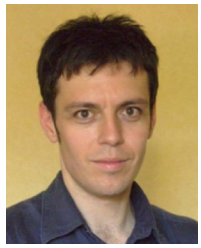

Frédéric Lamarque received the Ph.D. degree in electronics from the Universit Paris-Sud, Orsay, France, in 1998.

Since 2014, he has been a Full Professor of optics, and sensors and instrumentation with the Universit de Technologie de Compiègne (UTC), Compiègne, France. He was the Head of the Department of Mechanical Systems Engineering, UTC, from 2012 to 2016. He is a Member of the Laboratory of Excellence Control of Technological Systems-of-Systems (labex MS2T). Since 2015, he has been leading the MicroNanoSystems Group of UTC in the frame of the international network NAMIS (CNRS). His research interests include microsensors, microactuators, microrobotics, and opto-mechatronics.